Analytical Wake Modeling in Atmospheric Boundary Layers: Accounting for Wind Veer and Thermal Stratification

Journal of Physics: Conference Series **2767** (2024) 092018 doi:10.1088/1742-6596/2767/9/092018

Analytical Wake Modeling in Atmospheric Boundary Layers: Accounting for Wind Veer and Thermal Stratification

Ghanesh Narasimhan, Dennice F. Gayme, Charles Meneveau
Department of Mechanical Engineering, Johns Hopkins University, Baltimore, MD, 21218.
E-mail: ghanesh91@gmail.com

Abstract. Reliable characterization of wind turbine wakes in the presence of Atmospheric Boundary Layer (ABL) flows is crucial to accurately predict wind farm performance. Wind veering in the ABL shears the wake in the lateral direction, and wind veer strength depends on the thermal stability of the ABL. Analytical wake modeling approaches must capture these ABL effects to ensure correct prediction of the wake structure under varied atmospheric conditions. To this end, a new physics-based analytical wake model is developed in this study that is capable of predicting the shape of wakes influenced by wind veer and thermal stratification effects. This model combines a novel ABL wind field model with the Gaussian wake model. The new ABL wind model is capable of predicting both the streamwise and spanwise velocity components in conventionally neutral (CNBL) and stable (SBL) ABL flows. The analytical expressions for both of these horizontal velocity components adhere to Monin-Obukhov Similarity Theory (MOST) in the surface layer, while capturing wind veering in the outer layer of the ABL. Incorporating this ABL model with the Gaussian wake model predicts laterally deflected wake shapes in a fully predictive and self-consistent fashion for a wide range of atmospheric conditions. The results also demonstrate that the enhanced wake model gives improved predictions relative to Large Eddy Simulations of power losses due to wake interactions under strongly stably stratified atmospheric conditions, where wind veer effects are dominant.

1. Introduction

Wake interactions between wind turbines in an atmospheric boundary layer (ABL) exert a significant influence on the performance of wind farms. The analytical modeling of wind turbine wakes is challenging due to the influence of the Coriolis and buoyancy forces in the ABL. The Coriolis force causes wind direction changes, resulting in a sheared wake structure. The buoyancy forces associated with stable boundary layers (SBLs) cause more pronounced wind veer while they are absent in truly neutral boundary layer (TNBL) flows. Induced by the diurnal variations in the solar heating of the surface, wind farms encounter such stable atmospheric conditions quite often, marked by the formation of nocturnal low-level jets [1]. Consequently, such effects should be taken into account in the development of wind turbine wake models. While existing Gaussian-type wake models [2–4] only consider TNBL condition, an enhanced version of the Gaussian wake model is proposed in this study to analytically capture the wind turbine wake structures across different atmospheric conditions. Ref. [5] derived a new analytical ABL wind model that couples Ekman boundary layer flow descriptions with the Monin-Obukhov Similarity Theory (MOST) surface layer representation. This versatile model is valid for conventionally neutral (CNBL) and stable atmospheric conditions. The model predicts essential flow features, such as streamwise

and spanwise ABL velocity profiles, friction velocity (u_*), cross-isobaric angle (α_0), ABL height (h), and surface cooling flux (Q_0). Having fully analytical descriptions of ABL flows enables us to combine them with existing wind turbine wake models [2–4], and thus predict the wake structures in both CNBL and SBL flows. Section §2 discusses the corresponding improved wake modeling methodology. In Section §3, the configuration of Large Eddy Simulations (LES) carried out for comparing predictions from the ABL and wake models is briefly outlined. The validation of the wake model is demonstrated by showing good agreement of the model predictions for the velocity deficit with the corresponding LES cases in Section §4. Furthermore, the results in Section §4 show that the inclusion of the wind veer in the wake model [6, 7] improves the accuracy of downstream wind turbine power estimates compared to existing models. The main conclusions of this study are summarized in Section §5.

2. A comprehensive Gaussian wake model for wind turbine wakes in ABL flows

This section discusses an analytical wake model that can capture wake structures behind wind turbines under various atmospheric conditions in a self-consistent and fully predictive manner. The steady-state wake structure is represented using the Gaussian wake model proposed in Ref. [2]. Ref. [6] extended this Gaussian model by introducing a veer-correction term to account for the lateral deflection of wakes induced by wind veer in the ABL. However, since computing the veer correction term requires velocity profiles from LES as inputs, the veer-corrected wake model of Ref. [6] is not fully predictive and self-consistent. This problem is alleviated by integrating the veer-corrected Gaussian wake model with the novel ABL wind model proposed in Ref. [5]. The enhanced veer-corrected analytical Gaussian wake model is based on a Cartesian coordinate system where x, y, and z represent the streamwise, spanwise, and wall-normal directions, respectively. The origin of the coordinate system is located on the ground directly below the hub of the turbine. The wake model is based on the standard expression [2] for the streamwise velocity deficit $\Delta u(x,y,z) = U(z) - u(x,y,z)$, where $U(z)$ is the mean turbine inlet velocity in the streamwise direction and $u(x,y,z)$ is the streamwise component of the velocity field. In particular, Δu normalized by the ABL inflow velocity (U_h) at the hub height (z_h) is expressed as:

$$\Delta u(x,y,z)/U_h = C(x)\ \exp\left[-[(y-y_c(z))^2 + (z-z_h)^2]/2\sigma^2(x)\right]. \tag{1}$$

In Eq. (1), $C(x)$ is the magnitude of the maximum velocity deficit, as a function of streamwise distance from the turbine x, while $\sigma(x)$ determines the width of the wake structure. The lateral coordinate y_c denotes the spanwise-centroid location of the wake structure. The wake width $\sigma(x)$ is modeled as:

$$\sigma(x) = k_w x + 0.4R\sqrt{A_*}. \tag{2}$$

Here, R is the radius of the turbine rotor, A_* represents the ratio of the expanded stream tube area to the projected frontal area of the rotor, given by $A_* = (1+\sqrt{1-C_T})/(2\sqrt{1-C_T})$, where C_T is the thrust coefficient of the turbine. The width $\sigma(x)$ is assumed to expand linearly in the downstream direction with a wake growth rate k_w. Free stream turbulence in the ABL leads to the entrainment of momentum within the wake region. Consequently, the magnitude of the wake recovery rate depends on the turbulence intensity, denoted as $I_u = \sqrt{\langle u'u' \rangle}/U_h$. As shown in Ref. [8], the wake recovers faster in CNBL flows compared to SBL flows due to the higher turbulence intensity in CNBL flows. The decrease in I_u within SBLs is attributed to stable stratification within the boundary layer where turbulence destruction by buoyancy forces is dominant. Following the study for ABL flows with higher turbulence intensity, in Ref. [9], the wake growth rate is modeled as $k_w = 0.33\, I_u$. Similarly, for SBL flows with lower I_u, the growth rate is assumed to tend toward a constant value, $k_w = 0.021$, as shear-generated turbulence becomes dominant over turbulent entrainment mediated by ABL turbulence [9]. To model k_w across both low and high I_u regimes, the following empirical model for k_w is used [10]:

$$k_w = [0.021^n + (0.33I_u)^n]^{1/n}\,, \tag{3}$$

where $n = 6$ is determined based on obtaining a good match between the LES and model prediction for velocity deficit decay magnitude $C(x)$. The latter is given by:

$$C(x) = \begin{cases} 2a & ,x < x_0, \\ 1 - \sqrt{1 - C_T/[2\sigma^2(x)/R^2]} & ,x > x_0 \end{cases}. \tag{4}$$

Here, $a = (1/2)(1 - \sqrt{1 - C_T})$ is the induction factor, x_0 marks the transition location from the potential core region to the decaying region [10], which is expressed as:

$$x_0 = (R/k_w)\left[(1/\sqrt{2}) - (2/5)\sqrt{A_*}\right]. \tag{5}$$

From previous studies in Refs. [11–14], the streamwise variance of the turbulent fluctuations normalized by the square of the friction velocity (u_*) can be modeled as:

$$\langle\overline{u'u'}\rangle/u_*^2 = -A_1 \ln(z/h) + B_1, \tag{6}$$

where A_1 is the "Townsend-Perry constant" [13], assumed to be universal, and B_1 is a flow-dependent coefficient. Using Eq. (6), the I_u in Eq. (3) is modelled as:

$$I_u = [-A_1 \ln(z/h) + B_1]^{1/2}\,(u_*/U_h), \tag{7}$$

and $A_1 = 1.25$ based on Refs. [12–15]. The value of the flow-dependent constant B_1 is chosen as $B_1 = 0.6$ based on the current LES data. The values of u_*, h, and U_h in Eq. (7) are obtained from the new ABL wind model, which is discussed in the following text.

The z-dependent wake centroid spanwise location, y_c, constitutes the veer-correction term that models the veer-induced spanwise deformation at each height z as:

$$y_c(z) = V(z)\;[x/U(z)]. \tag{8}$$

Here, $V(z)$ is the spanwise velocity component of the ABL inflow. Ref. [6] obtained the ABL velocity profiles from LES data, rendering the wake model not analytically self-contained. However, in this study, the analytical ABL wind model derived in Ref. [5] is utilized rather than the LES-generated profiles. The model expressions for the $U(z)$ and $V(z)$ ABL velocity components are obtained for a given latitude (ϕ) in the northern hemisphere. They depend on the Coriolis frequency $f_c = 2\Omega\sin\phi$, where $\Omega = 7.27 \times 10^{-5}$ 1/s is the Earth's rotation rate. The corresponding model expressions for the ABL inflow velocities as the function of the dimensionless wall-normal height $\hat{\xi} = zf_c/u_*$ are given by:

$$\frac{U(\hat{\xi})}{u_*} = \begin{cases} -g'(\hat{\xi})\left[1 - (\hat{\xi}/\hat{h})\right]^{3/2} + [3g(\hat{\xi})/2\hat{h}]\sqrt{1 - (\hat{\xi}/\hat{h})} + U_g/u_*, & \hat{\xi} \geq \hat{\xi}_m \\ \kappa^{-1}\ln(\hat{\xi}/\hat{\xi}_0) + (5\mu + 0.3\mu_N)(\hat{\xi} - \hat{\xi}_0) & ,\quad \hat{\xi} \leq \hat{\xi}_m \end{cases}, \tag{9}$$

$$\frac{V(\hat{\xi})}{u_*} = \frac{g(\hat{\xi})g'(\hat{\xi})}{[1 - g(\hat{\xi})^2]^{1/2}}\left[1 - (\hat{\xi}/\hat{h})\right]^{3/2} + (3/2\hat{h})\sqrt{1 - g(\hat{\xi})^2}\left[1 - (\hat{\xi}/\hat{h})\right]^{1/2} + V_g/u_*. \tag{10}$$

In these equations, $\kappa = 0.41$ is the Von-Kármán constant, while $\hat{\xi}_0 = z_0 f_c/u_*$, and $\hat{h} = hf_c/u_*$ are the dimensionless surface roughness and ABL heights, respectively. The terms $U_g = G\cos\alpha_0$ and $V_g = G\cos\alpha_0$ denote the Geostrophic wind velocities, which depend on the Geostrophic wind magnitude, $G = \sqrt{U_g^2 + V_g^2}$, and cross-isobaric angle, $\alpha_0 = \tan^{-1}(V_g/U_g)$. A simple change in sign for $V(z)$ and V_g would give the ABL structure for the southern hemisphere. The functions $g(\hat{\xi})$ and $g'(\hat{\xi})$ are given by:

$$g(\hat{\xi}) = c_g\left(1 - e^{-\hat{\xi}/\Gamma\hat{h}}\right), \qquad g'(\hat{\xi}) = \left(c_g/\Gamma\hat{h}\right)e^{-\hat{\xi}/\Gamma\hat{h}}, \tag{11a,b}$$

where, $c_g = 1.43$, $\Gamma = 0.83$ are model constants obtained from LES. The $U(\hat{\xi})$ profile given by Eq. (9) comprises two distinct layers: the outer and inner layers. The outer layer velocity is determined by the classic 3/2 power law profile for the total stress $\hat{\mathrm{T}} = \sqrt{\hat{\mathrm{T}}_{xz}^2 + \hat{\mathrm{T}}_{yz}^2} = [1-\hat{\xi}/\hat{h}]^{3/2}$ [16], where $\hat{\mathrm{T}}_{xz}, \hat{\mathrm{T}}_{yz}$ are the turbulent shear stress components in the streamwise and spanwise directions, respectively. The inner layer velocity follows the MOST profile, capturing the classic Atmospheric Surface Layer (ASL) characteristics. These two velocity layers are matched at a height denoted as $\hat{\xi}_m$, which is set to 20% of the ABL depth ($\hat{h}$). The calculation of $\hat{h}$ follows an equilibrium boundary layer depth model [17] given by:

$$\hat{h}^{-2} = C_{TN}^{-2} + C_{CN}^{-2}\ \mu_N + C_{NS}^{-2}\ \mu. \tag{12}$$

Here, the model constants $C_{TN} = 0.5$, $C_{CN} = 1.6$ are obtained by fitting the modeled $\hat{h}$ with height data from the LES of CNBL flows in Ref. [18]. Similarly, the constant $C_{NS} = 0.78$ is obtained by fitting the expression for ABL height with measurements from the LES data of SBL flows described in Ref. [5]. The Monin-Kazanski stability parameter $\mu = u_*/\kappa f_c L_s$ and the Zilitinkevich number $\mu_N = N_\infty/f_c$ in equations (9), (12) account for the effects of surface cooling and the thermal stratification strength of the free stream, respectively. Here, $L_s = -u_*^3/(\kappa[g/\Theta_0]Q_0)$ is the Obukhov length, where $g = 9.81$ m/s^2 is the gravitational acceleration, Θ_0 is the reference potential temperature. The quantity $N_\infty = \sqrt{[g/\Theta_0]\gamma_\Theta}$ is the Brunt-Väisälä frequency of the free geostrophic flow with γ_Θ denoting the vertical gradient of the potential temperature. For a quasi-steady flow, the surface cooling flux can be modeled as $Q_0 = C_r h$, where C_r is the cooling rate of the surface potential temperature. Furthermore, for a given Geostrophic wind velocity magnitude G, the components U_g, V_g, and u_* are obtained from a new Geostrophic drag law (GDL) model that is self-consistently derived from enforcing continuity in the model velocity profiles at the matching location $\hat{\xi} = \hat{\xi}_m = c_m\hat{h}$ with $c_m = 0.2$. The new form of the GDL model expressions are:

$$\kappa U_g/u_* = \ln\left(u_*/f_c z_0\right) - A, \qquad \kappa V_g/u_* = -B, \tag{13a,b}$$

where the GDL constants A and B are evaluated as:

$$A = -\ln c_m\hat{h} - \kappa\left[(5\mu + 0.3\mu_N)(c_m\hat{h} - \hat{\xi}_0) + g'(\hat{\xi}_m)\left(1 - c_m\right)^{3/2} - g(\hat{\xi}_m)(3/2\hat{h})\sqrt{1 - c_m}\right], \tag{14}$$

$$B = 3\kappa/2\hat{h}. \tag{15}$$

In summary, the new enhanced version of the wake model is obtained by integrating the Gaussian wake model from Eq. (1) with the ABL model expressions, Eqs. (9) and (10). The models are coupled through the veer-correction term given by Eq. (8). This improved version of the wake model described in this section can predict different wake structures for various atmospheric conditions covering both the CNBL and SBL regimes. The additional model predictions for u_*, U_g, V_g from the new GDL model are represented by Eqs. (13a,b), (14) & (15), ABL height h from Eq. (12), and a model for surface cooling flux given by $Q_0 = C_r h$, makes the wake model entirely self-contained. This feature eliminates the need for external inputs to evaluate the wake model, ensuring a comprehensive and self-consistent predictive model [5].

3. Description of LES data used for model development and validation

In this section, a concise overview of the LES employed in constructing and testing the ABL wind and wake models is provided. More detailed information about the LES for CNBL and SBL flows can be found in Ref. [5]. Simulations use the LESGO code [19] that solves the filtered Navier-Stokes equations and potential temperature equation in an x, y, z Cartesian coordinate system. The pseudo-spectral method is used in the horizontal directions, while a

centered second-order finite difference method is used along the vertical direction. The sub-grid stress (SGS) tensor is modeled using the scale-dependent Lagrangian dynamic model [20]. The computational domain size is $L_x \times L_y \times L_z = 3.75$ km $\times$ 1.5 km $\times$ 2 km, and it is discretized using $N_x \times N_y \times N_z = 360 \times 144 \times 432$ grid points corresponding to a grid resolution of $\Delta x \times \Delta y \times \Delta z = 10.4$ m $\times$ 10.4 m $\times$ 4.6 m. Boundary conditions comprise wall stress from the MOST-based equilibrium wall model at the bottom wall and stress-free conditions at the top wall. Momentum and scalar surface roughness heights in the wall model equations are defined as $z_0 = 0.1$ m and $z_{0s} = 0.1 z_0$.

Initially, the LES of CNBL flow is performed by setting the potential temperature with a linear gradient profile $\Theta(z) = \Theta_0 + \gamma_\Theta z$ with $\gamma_\Theta = \partial\Theta/\partial z = 1$ K/km and surface potential temperature $\Theta_0 = 265$ K. The velocity field is initiated with a log-law profile near the bottom boundary, merging with a uniform velocity of magnitude $G = 15$ m/s. The Coriolis frequency is set to $f_c = 10^{-4}$ 1/s. To induce turbulence, a zero-mean white noise superposed with the mean velocity profiles is introduced within the first 100 m from the bottom surface. The potential temperature equation is subject to a zero heat flux boundary condition. As a result of this insulating boundary condition, the initial linear potential temperature profile evolves into a CNBL profile, characterized by a neutrally stratified boundary layer region separated from the stable free stream region by a capping inversion layer. To conduct LES of the SBL flow, the scalar equation is initialized with the steady-state CNBL potential temperature profile. The initial velocity condition remains consistent with that used for CNBL flow LES. To induce SBL flow, the bottom surface is cooled by decreasing the surface potential temperature at a specified cooling rate C_r (K/hr). Various SBL conditions are simulated with cooling rates $C_r = [-0.03, -0.125, -0.25, -0.375, -0.5, -1]$ K/hr, which are referred as SBL-1 to 6, respectively here and in Ref. [5]. Once the CNBL and SBL simulations reach a quasi-steady state, temporal and spatial averaging are performed to obtain the mean vertical structures of the velocity, temperature, and turbulent shear stress components. The mean profiles of turbulent shear stress from LES are utilized to motivate the development of the new ABL wind model in Eqs. (9) and (10). This new analytical ABL model can predict mean velocity profiles for CNBL and SBL flows that agree well with the LES results, as shown in Figure 1. While the traditional MOST model captures the log layer and the stability-affected region within the ASL, it significantly deviates from the LES velocity outside the surface layer. The MOST method also does not model the veering wind in the ABL, as it describes only the resultant wind velocity magnitude. On the other hand, the new ABL model captures both the streamwise and spanwise velocity components not only within the ASL but throughout the flow domain. The model also additionally provides self-consistent predictions for the values of friction velocity (u_*), Geostrophic velocities (U_g, V_g) through GDL Eqs. (13a,b), (14), (15), and the ABL height (h) from Eq. (12). The validation of the GDL and ABL height model equations is thoroughly discussed in Ref. [5].

The concurrent-precursor method [7, 21] is utilized to obtain relevant LES data for validating the wake model. The precursor domain consists of CNBL and SBL simulations performed without a wind turbine. In the wind turbine domain, a wind turbine is positioned 500 m from the domain inlet. The turbine is represented using the Actuator Disc Method (ADM) with a thrust coefficient set to $C_T = 0.75$, diameter $D = 2R$, and hub height z_h both set to 100 m. A schematic representation of this setup is available in Figure 1 of Ref. [7]. As the simulations reach a quasi-steady state, the time-averaging of the 3D velocity fields is performed in the wind turbine domain. These time-averaged fields are used for the construction and validation of the wake model discussed in Section §2.

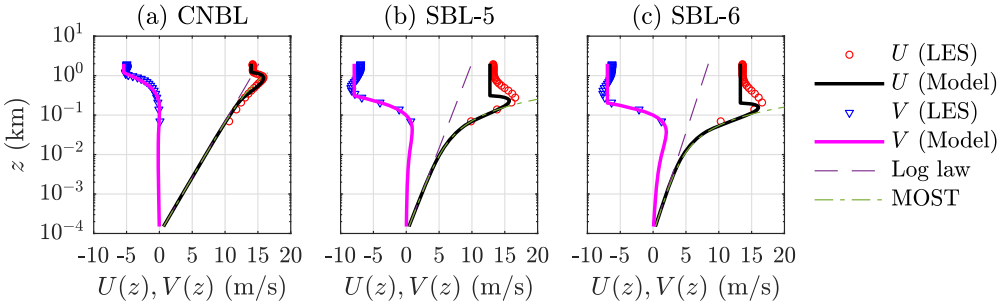

Figure 1. Comparison of LES vs model predictions of $U(z)$ and $V(z)$ for: (a) CNBL, (b) SBL-5 ($C_r = -0.5$ K/hr), (c) SBL-6 ($C_r = -1$ K/hr) flows.

4. Results and discussion

In this section, the validation of the new enhanced wake model is presented by comparing its predictions with LES results. For comparisons of model predictions with LES, only the TNBL, CNBL, SBL-5, and SBL-6 cases from Ref. [5] are considered. The choice of these specific cases is to demonstrate the model's ability to capture wind veer effects by comparing wake model predictions between scenarios with less wind veer (TNBL, CNBL) and those dominated by wind veer (SBL-5, SBL-6). The performance of the model is assessed through comparisons of the centerline velocity deficit decay $C(x)$ in Section §4.1. Then the model's accuracy is evaluated by comparing predictions of $\Delta u(x, y, z)/U_h$ at various x-cross-plane locations with LES in Section §4.2. Finally in Section §4.3, the power loss predictions from the wake model are compared with LES results, focusing on the power generated by hypothetical turbines placed at various locations in the sheared wakes for the various cases.

4.1. Centerline velocity deficit decay

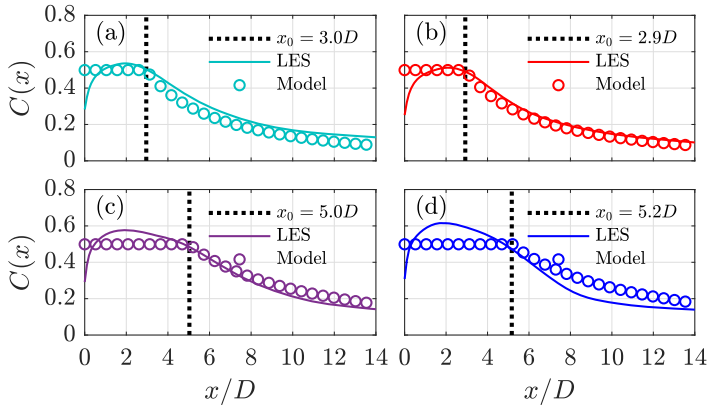

Figure 2. Plot of $C(x)$ vs x/D from Eq. (4) compared against corresponding LES results for (a) TNBL, (b) CNBL, (c) SBL-5, and (d) SBL-6 cases.

Figure 2(a)-(d) presents the comparison of $C(x)$ from Eq. (4) with corresponding LES results for the TNBL, CNBL, SBL-5, and SBL-6 cases, respectively. The model predictions, indicated by the circle markers for each case, align well with LES results. Additionally, the plots illustrate that the prediction for the transition location x_0 given by Eq. (5) accurately distinguishes the potential core region from the decay region. According to Eq. (5), x_0 is inversely proportional to k_w. As the wake expands more slowly for the SBL cases, longer potential core regions and consequently longer wake structures are observed for SBL flows.

4.2. Wake velocity contours at various downstream distances

Contour plots of the velocity deficit normalized by the ABL velocity at hub height, $\Delta u/U_h$, are displayed in Figure 3. The contours are presented for five different downstream locations at $x/D = [1, 3, 5, 8, 11]$. In each panel, the blue circles indicate the turbine rotor edge. Figures 3 (a), (c), (e), and (g) depict wake contours from LES for cases TNBL, CNBL, SBL-5, and SBL-6, respectively. Corresponding model predictions from Eq. (1) are shown in Figures 3 (b), (d), (f), and (h). The wake contours from LES reveal that the wind veer effect is more prominent for the SBL-5 and SBL-6 cases, where the wakes exhibit lateral shear.

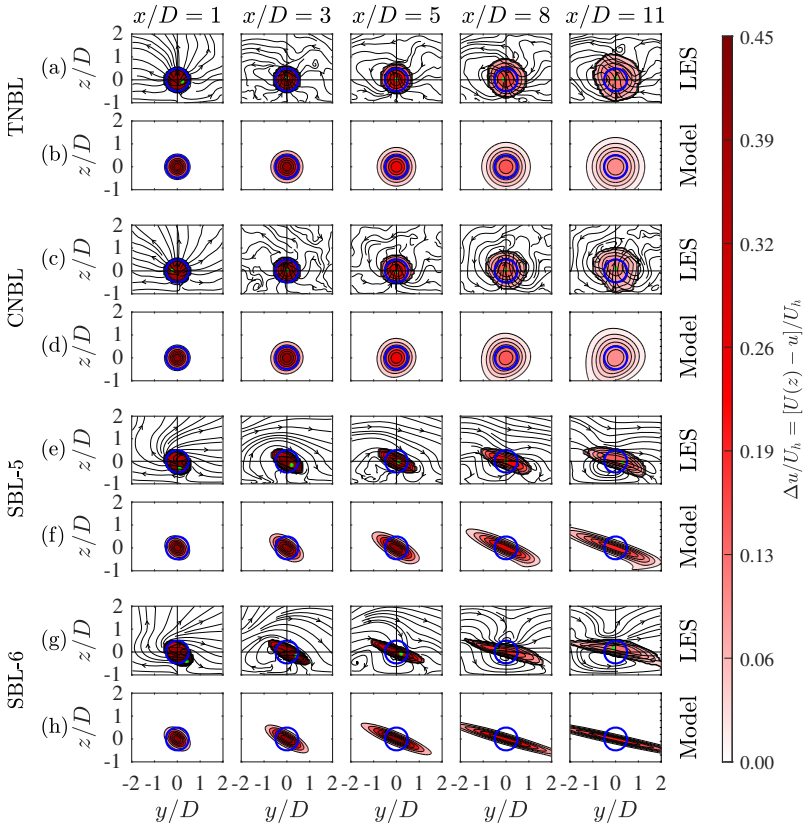

Figure 3. Contours of $\Delta u/U_h$ from Eq. (1) compared against LES contours with cross-stream (v-w) velocity streamlines. The green marker denotes the maximum deficit location. The blue circle represents the rotor edge of the turbine.

In contrast, for neutral ABL flows (TNBL & CNBL cases), the wake structure exhibits a symmetric distribution around the turbine hub. The contours from the analytical wake model closely resemble the LES results. The model reproduces symmetric wake shapes for neutral conditions, while capturing tilted wake structures for SBL flows. The wake decay characteristics predicted by the wake model are also similar to their LES counterparts. Although the model successfully captures key features like symmetric or sheared wake structures, minor variations in wake shape do exist compared to LES. For example, the model assumes the peak velocity deficit to always occur at the rotor center. However, it does not strictly lie at the origin as shown by the green markers in LES results. These minor deviations stem from cross-stream advection of the wake due to secondary flows as shown in LES contours. The wake model does not account for these secondary flow features. However, it still offers a good approximation of the wake distribution at a lower cost than LES.

4.3. Quantifying power loss due to wake interactions

In this section, the enhanced wake model is used to quantify the power loss from wake interactions. The power output of a wind turbine is proportional to the cube of the velocity, averaged over the rotor disc area. To calculate the velocity downstream of the wind turbine, the velocity deficit Δu predicted by the wake model is subtracted from the streamwise velocity at the rotor disk, $U(z)$ obtained from the ABL model, i.e., $u(x, y, z) = U(z) - \Delta u(x, y, z)$. Contours of the velocity at $x/D = [1, 3, 5, 8, 11]$ behind a wind turbine placed in the SBL-6 condition are shown in Figure 4. Contours from LES are depicted in Figure 4(a) while Figures 4(b) and (c) are predictions from the wake model. In Figure 4(b), Δu is computed from the wake model including the veer correction term y_c (Eq. 8), and is referred to as M-1 in the figure. Similarly, Figure 4(c) shows contours evaluated using the wake model without the veer correction term ($y_c = 0$), referred to as M-2 in the figure. It is evident that $u(x, y, z)$ predicted using the M-1 model has a better qualitative agreement with LES compared to the M-2 model. These results underscore the importance of incorporating the spanwise veer deflection term in the wake model.

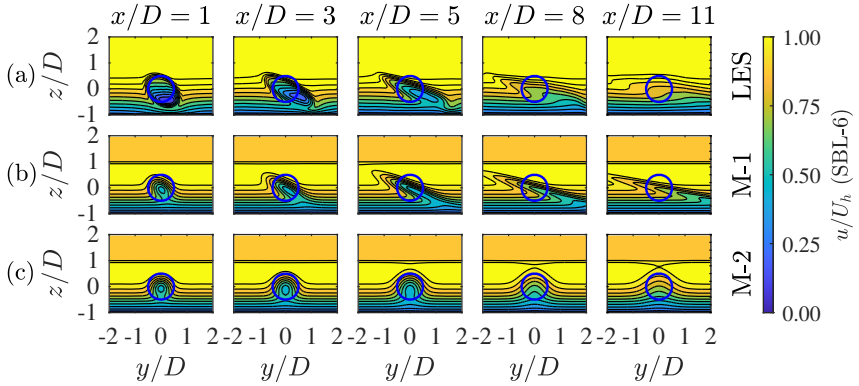

Figure 4. Contours of $u(x, y, z)/U_h$ behind a wind turbine placed in the case SBL-6 flow plotted from (a) LES, Δu from Eq.(1) (b) with $y_c(z) = V(z)\,[x/U(z)]$ (Eq. 8) (M-1), & (c) $y_c = 0$ (M-2).

Next, the power loss due to wake interactions is quantified by defining the ratio $P(x_T, y_T)/P_0$. Here, $P(x_T, y_T)$ represents the power output of a hypothetical wind turbine placed at a specific location marked by the coordinate x_T, y_T behind an upstream wind turbine. Similarly, P_0 is the power output of the wind turbine placed in an unobstructed ABL flow. The power ratio $P(x_T, y_T)/P_0$ can be expressed as:

$$P(x_T, y_T)/P_0 = \left[(1/\pi R^2 U_h) \int_y \int_z [U(z) - \Delta u(x_T, y - y_T, z)]\ dy\ dz \right]^3 . \tag{16}$$

Figures 5(a), (b), (c), & (d) show the power ratios of a wind turbine placed in TNBL, CNBL, SBL-5, and SBL-6 ABL flows, respectively. The figures show the spanwise profiles of power ratios for a wind turbine placed at $x_T/D = [4, 6, 8, 10]$. The circle markers represent the power ratios from LES. The red solid line and blue dash-dotted line are predictions of the power ratios using the M-1 and M-2 wake models, respectively. Upon comparing power ratios in neutral and stable atmospheric conditions, it becomes apparent from the figures that the power ratio predictions from the M-1 model exhibit better agreement with LES results than the M-2 model for the SBL-5 and SBL-6 cases. In the far-downstream locations for the SBL-5 case, the mean absolute percentage errors of model predictions relative to LES are 5% and 6% for evaluating Eq. (16) using M-1 and M-2 models, respectively. Meanwhile, for the SBL-6 case, the corresponding errors are 5% and 10% with the M-1 and M-2 models, respectively. However, both models predict similar power ratio profiles for neutral conditions (TNBL & CNBL) that align well with LES

data. This analysis reveals that the new enhanced wake model, which considers veer effects, performs better in predicting power loss due to wake interactions compared to the Gaussian wake model without veer correction. The improvement is observed across a broad range of atmospheric conditions.

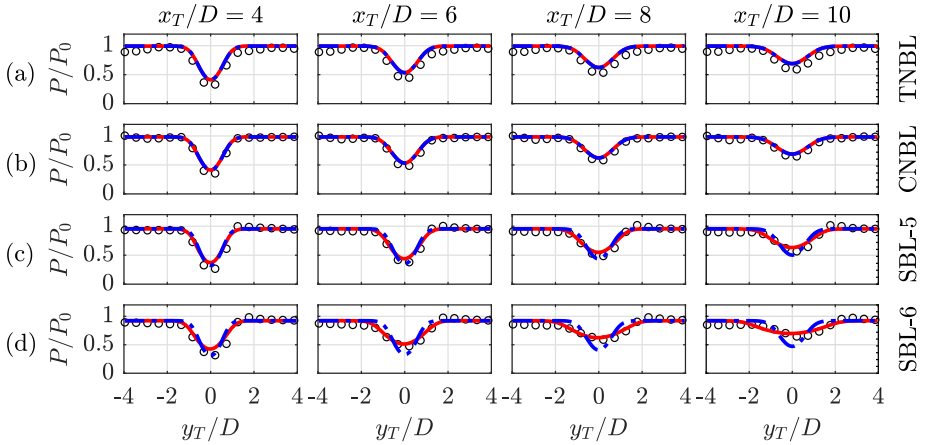

Figure 5. Plots of power ratio P/P_0 (Eq. 16) at locations $x_T/D = [4, 6, 8, 10]$ from M-1 (—) & M-2 (-·-) compared against LES (○): (a) TNBL, (b) CNBL, (c) SBL-5, and (d) SBL-6.

5. Conclusions

In summary, a novel physics-based wake modeling methodology is introduced in this study. It predicts wake structures across a broad range of atmospheric conditions. The enhanced wake model is achieved by integrating the new ABL wind model derived in Ref. [5] with the veer-corrected Gaussian wake model proposed in Ref. [6]. The ABL wind model provides analytical predictions for the entire vertical structure of CNBL and SBL flows. It also offers predictions for the friction velocity (u_*), ABL height (h), and the cross-isobaric angle (α_0) through a new form of the Geostrophic Drag Law model [5]. These ABL flow predictions are achieved in a self-consistent and fully predictive manner, ensuring that the wake model, when integrated with the ABL model, also remains self-consistent and fully predictive. Consequently, the wake model can accurately predict wake structures across a wide range of atmospheric conditions at a lower cost than LES. In the wake model, a new model for the wake expansion rate (k_w) is also included, which assumes dependence on the turbulence intensity I_u of the flow and relates the latter to a generalized version of the logarithmic law of variance of streamwise velocity fluctuations in boundary layers [11–15]. The modeled k_w effectively captures wind turbine wakes with a slower growth rate for low-I_u SBL flows and a faster wake expansion rate for high-I_u CNBL flows. This approach to modeling k_w ensures good prediction of the velocity deficit magnitude decay $C(x)$ for a broad range of atmospheric conditions. It has also been illustrated that the new enhanced wake model, incorporating a self-consistent veer correction, provides better predictions of power loss resulting from wake interactions. This new model outperforms existing wake models that either neglect veer effects entirely or require external inputs to calculate veer-induced wake shape deformations. The new wake model in this study is derived under the assumption of a smooth wall and the presence of a single un-yawed turbine in the ABL. As a future scope for this study, further modeling efforts are needed to address more general scenarios, including modeling of wakes behind yawed turbines (see initial efforts in [10]), and their interactions in a wind farm. Moreover, to provide a more comprehensive representation of real-world conditions, it is essential to include considerations for non-smooth walls, such as canopy flows [22], marine ABLs with sea/ocean wave effects [23], etc.

6. Acknowledgements
This work is supported by the NSF grants CBET-1949778 and CMMI-2034111. We are grateful for the HPC support from Cheyenne (DOI: 10.5065/D6RX99HX), provided by NCAR's CISL and sponsored by the NSF, and the ARCH core facility (rockfish.jhu.edu), supported by NSF grant OAC1920103.

References
[1] D. L. Rife et al. "Global Distribution and Characteristics of Diurnally Varying Low-Level Jets". In: Journal of Climate 23.19 (2010), pp. 5041–5064.

[2] M. Bastankhah and F. Porté-Agel. "A new analytical model for wind-turbine wakes". In: Renewable Energy 70 (2014), pp. 116–123.

[3] M. Bastankhah and F. Porté-Agel. "Experimental and theoretical study of wind turbine wakes in yawed conditions". In: J. of Fluid. Mech. 806 (2016), pp. 506–541.

[4] M. Bastankhah et al. "A vortex sheet based analytical model of the curled wake behind yawed wind turbines". In: J. of Fluid Mech. 933 (2022), A2.

[5] G. Narasimhan et al. "Analytical Model Coupling Ekman and Surface Layer Structure in Atmospheric Boundary Layer Flows". In: Boundary-Layer Meteorology 190.4 (2024), p. 16.

[6] M. Abkar et al. "An Analytical Model for the Effect of Vertical Wind Veer on Wind Turbine Wakes". In: Energies 11.7 (2018).

[7] G. Narasimhan et al. "Effects of wind veer on a yawed wind turbine wake in atmospheric boundary layer flow". In: Phys. Rev. Fluids 7 (2022), p. 114609.

[8] M. Abkar and F. Porté-Agel. "Influence of atmospheric stability on wind-turbine wakes: A Large Eddy Simulation study". In: Physics of Fluids 27.3 (2015), p. 035104.

[9] D. Vahidi and F. Porté-Agel. "A physics-based model for wind turbine wake expansion in the atmospheric boundary layer". In: J. of Fluid. Mech. 943 (2022), A49.

[10] G. Narasimhan. "Enhancing Wind Turbine Wake Modeling in Atmospheric Boundary Layers: Insights into Veer and Thermal Stratification Effects". Retrieved from https://jscholarship.library.jhu.edu/handle/1774.2/69145. Doctoral dissertation. Baltimore, MD: Johns Hopkins University, 2023.

[11] I. Marusic and G. J. Kunkel. "Streamwise turbulence intensity formulation for flat-plate boundary layers". In: Physics of Fluids 15.8 (2003), pp. 2461–2464.

[12] M. Hultmark et al. "Turbulent Pipe Flow at Extreme Reynolds Numbers". In: Phys. Rev. Lett. 108 (9 2012), p. 094501.

[13] I. Marusic et al. "On the logarithmic region in wall turbulence". In: J. of Fluid. Mech. 716 (2013), R3.

[14] C. Meneveau and I. Marusic. "Generalized logarithmic law for high-order moments in turbulent boundary layers". In: J. of Fluid. Mech. 719 (2013), R1.

[15] R. J. A. M. Stevens et al. "Large-eddy simulation study of the logarithmic law for second- and higher-order moments in turbulent wall-bounded flow". In: J. of Fluid. Mech. 757 (2014), pp. 888–907.

[16] F. T. M. Nieuwstadt. "The Turbulent Structure of the Stable Nocturnal Boundary Layer". In: J. of Atmos. Sci. 41.14 (1984), pp. 2202–2216.

[17] S. Zilitinkevich and I. Esau. "Resistance and heat-transfer laws for stable and neutral planetary boundary layers: Old theory advanced and re-evaluated". In: Q.J.R. Meteorol. Soc. 131 (2005), pp. 1863–1892.

[18] L. Liu et al. "Geostrophic drag law for conventionally neutral atmospheric boundary layers revisited". In: Q. J. R. Meteorol. Soc. 147.735 (2021), pp. 847–857.

[19] https://lesgo.me.jhu.edu.

[20] E. Bou-Zeid et al. "A scale-dependent Lagrangian dynamic model for Large Eddy Simulation of complex turbulent flows". In: Physics of Fluids 17.2 (2005), p. 025105.

[21] R. J. Stevens et al. "A concurrent precursor inflow method for Large Eddy Simulations and applications to finite length wind farms". In: Renewable Energy 68 (2014), pp. 46–50.

[22] E. Patton et al. "Atmospheric stability influences on coupled boundary layer and canopy turbulence". In: Journal of the Atmospheric Sciences 73.4 (2016), pp. 1621–1647.

[23] P. P. Sullivan et al. "Large-Eddy Simulation of Marine Atmospheric Boundary Layers above a Spectrum of Moving Waves". In: Journal of the Atmospheric Sciences 71.11 (2014), pp. 4001–4027.